

In-Situ Synthesis of CQDs/BiOBr Material via Mechanical Ball Milling with Enhanced Photocatalytic Performances

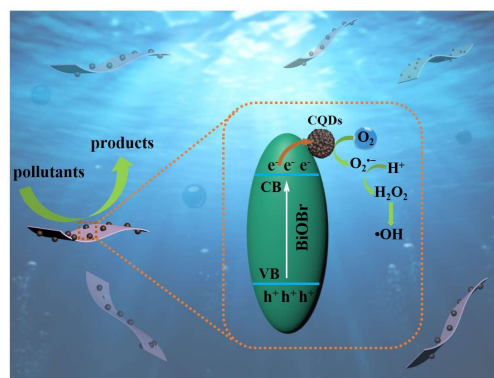
Xingwang Yan², Bin Wang², Mengxia Ji², Qi Jiang², Gaopeng Liu², Pengjun Liu^{1*}, Sheng Yin², Huaming Li² and Jiexiang Xia^{2*}

¹Key Laboratory of Medicinal and Edible Plants Resources of Hainan Province, Hainan Vocational University of Science and Technology, Haikou 571126, China

²School of Chemistry and Chemical Engineering, Institute for Energy Research, Jiangsu University, Zhenjiang 212013, China

ABSTRACT Designing simple, efficient, and environmentally friendly methods to construct high-efficient photocatalysts is an important strategy to promote the further development of the field of photocatalysis. Herein, flower-like carbon quantum dots (CQDs)/BiOBr composite photocatalysts have been prepared via in-situ synthesis by mechanical ball milling in the existence of ionic liquid. The CQDs/BiOBr composites exhibit higher photo-degradation performance for tetracycline (TC) than BiOBr monomer and the commercial Bi₂O₃ under visible light irradiation. For comparison, the different Br sources and synthetic methods are chosen to prepare BiOBr and CQDs/BiOBr composites. Photocatalysts prepared by ball milling and ionic liquid present significantly enhanced photocatalytic performance for removing TC. In addition, the introduction of CQDs could distinctly enhance the photocatalytic performances of pure BiOBr. The reason is that CQDs as electron acceptor effectively separate electrons and holes and inhibit their recombination. The intermediates during photocatalytic degradation were tested using liquid chromatography-mass spectrometry (LC-MS) and possible degradation pathways were given. During degradation, $\cdot\text{OH}$, $\text{O}_2^{\cdot-}$ and h^+ were identified to be the main active species based on electron spin resonance (ESR) spectra and free radical trapping experiments. A possible mechanism of CQDs/BiOBr with enhanced photocatalytic performances was further proposed.

Keywords: CQDs, BiOBr, photocatalysis, pollutant degradation



INTRODUCTION

In recent years, a large amount of substandard waste water including antibiotics and dyes has been directly discharged into rivers, causing serious water pollution problems and great damage to the natural environment which human beings depend on.^[1,2] How to effectively treat these waste water and repair the environment has become an urgent problem. As a simple, efficient and secondary pollution-free oxidation technology, semiconductor photocatalysis technology has been demonstrated to be a pollution-free and effective solution. It has a great application prospect in the treatment of waste water.^[3-5] However, most of semiconductor materials have problems with low sunlight utilization and the intense recombination of photogenerated carriers.^[6,7] How to improve the efficiency of photocatalytic degradation of semiconductor materials is the biggest challenge currently.

As a member of V-VI-VII ternary compounds, BiOBr (bismuth oxybromide) is a new type of semiconductor photocatalyst with the advantages of suitable position of energy band and strong light absorption capability.^[8,9] In addition, BiOBr presents a two-dimensional layered structure with a larger specific surface area and adsorbs more contaminants during the process of degradation.^[10-13] It attracts much attention for its unique physical and chemical properties in recent years. Shi et al.^[14] synthesized BiOBr nanosheets with two specific exposed facets, which showed excellent performance of photocatalytic water splitting. Wu et al.^[15]

prepared BiOBr monatomic layer photocatalysts with large oxygen vacancies with good photocatalytic CO₂ reduction properties. Despite the BiOBr photocatalytic material showing good photocatalytic properties in photocatalytic field, BiOBr still exhibits low charge utilization efficiency and weak visible light absorption, so the overall photocatalytic capability is limited.^[16,17] For the purpose of enhancing their photocatalytic properties, various modification strategies are used in the BiOBr photocatalytic system including bismuth-rich strategy,^[18,19] morphology control,^[20,21] heterostructures,^[22,23] element doping,^[24] defect engineering,^[25,26] etc. Semiconductor quantum dots (QDs) possess high light-capturing capability, tunable optical and electronic properties, and good stability. In particular, as carriers for photons, quantum dots can realize highly efficient photon-to-electron conversion. Therefore, semiconductor quantum dots show great prospects in the field of photocatalysis.^[27,28] As a new carbon nanomaterial, CQDs have the advantages of wide source and low cost. CQDs have been applied in photoconversion, biological imaging and luminescence devices due to their strong fluorescence.^[29,30] Recent studies show that CQDs have excellent interfacial electron transfer capability with good optical capture capability and are a good photocatalytic material. The introduction of a few CQDs to modify the semiconductor photocatalyst can effectively enhance the activity of the photocatalytic materials.^[31-34] Furthermore, relevant reports on the synthesis of CQDs/BiOBr composites by ionic liquid assisted mechanical ball milling method are extremely rare (Table

S1). Therefore, we believed that it could be attempted to introduce a few CQDs in the synthesis of BiOBr by mechanical ball milling to synthesize composites with better photocatalytic activity.

In this work, we constructed the CQDs/BiOBr composites in situ by ionic liquid assisted mechanical ball milling synthesis. The photocatalytic properties of BiOBr and CQDs/BiOBr synthesized by different methods and different Br sources were also compared. The effects of the introduction of CQDs on the material were discussed through a series of characterizations. Furthermore, the mechanism of enhanced photocatalytic performance was further investigated by identifying the main active species during degradation through the experiments of free radical capture and ESR spectra.

RESULTS AND DISCUSSION

The characterization of XRD aimed to ascertain crystal structure and composition of BiOBr monomer and CQDs/BiOBr composites. As seen from Figure 1a, all the peaks of as-prepared BiOBr could be well matched to BiOBr (JCPDS, No. 73-2061) with no offset and extra peaks. This indicated that the prepared BiOBr had high purity. In contrast with pure BiOBr, the various peaks of composites were broadened after the introduction of CQDs. The wide characteristic peaks became more and more obvious with the amount of CQDs increasing. The crystal growth of BiOBr was affected by CQDs, which revealed a strong interaction between BiOBr and CQDs. The characteristic diffraction peaks of CQDs were not found in the XRD plot of CQDs/BiOBr composites because of the small amount and high dispersion of CQDs in the materials. In order to study the structure and chemical bonds of the material, FT-IR analysis was performed on the synthesized materials. Figure 1b displays the FT-IR spectra of pure BiOBr and CQDs/BiOBr composites. Clearly, all of the materials have a characteristic peak at 527 cm^{-1} , which corresponds to the Bi-O stretching mode of BiOBr.^[35] In the CQD/BiOBr composites, new absorption peaks appear at 812 , 1090 and 1470 cm^{-1} belonging to the bending vibration of C-H bonds, stretching vibration of C-O bonds and sym-

metric stretching of C-C, respectively.^[36-38] Therefore, it could be determined that CQDs have been successfully loaded on the monomer of BiOBr and constructed excellent combination.

The exterior chemical states and element compositions of synthesized material were analyzed and studied by XPS. Figure S1 exhibits the survey scan XPS spectrum of the prepared materials, which clearly indicated the existence of Bi, O and Br in BiOBr and CQDs/BiOBr composites. It suggested no other impurities were present in the samples. As observed from Figure 1c, two characteristic peaks at 159.3 and 164.6 eV were attributed to Bi $4f_{7/2}$ and Bi $4f_{5/2}$ by Bi^{3+} species.^[23] Figure 1d shows an obvious peak with the binding energy at 530.2 eV corresponding to O $1s$.^[39] Furthermore, the characteristic peak of Br $3d$ at 68.5 eV could also be observed clearly in Figure 1e.^[40] In the CQDs/BiOBr composites, the binding energy of Bi and Br elements was slightly increased compared with that of the BiOBr monomer, because the introduction of CQDs changed the chemical environment of surface around Bi and Br. Therefore, there are interaction forces between CQDs and BiOBr. The XPS spectra of C $1s$ are presented in Figure 1f. The representative peak of C $1s$ is at 284.6 eV corresponding to external carbon source while other typical peaks at 286.0 and 288.1 eV were attributed to C-O bonds and C=O functional groups,^[39] respectively. It demonstrated CQDs had been successfully introduced into BiOBr according to the above results.

To investigate the effects of introducing CQDs on the size and morphologies of prepared catalysts, they were investigated by SEM, TEM and HRTEM. Figure 2a is a TEM image of the BiOBr monomer, which showed that the BiOBr exhibits ultrathin nanosheet structure. This sheet structure exposed a large area, which not only improved the utilization of material, but also adsorbed more pollutants in the photocatalytic reaction. After introducing CQDs, the morphology of the sample changed significantly. BiOBr nanosheet appeared agglomeration, presenting microflower structure about $200\text{--}300\text{ nm}$. The superficies of CQDs/BiOBr composites also became much rougher (Figure 2b and c). Furthermore, CQDs with the size of 5 nm could be clearly ob-

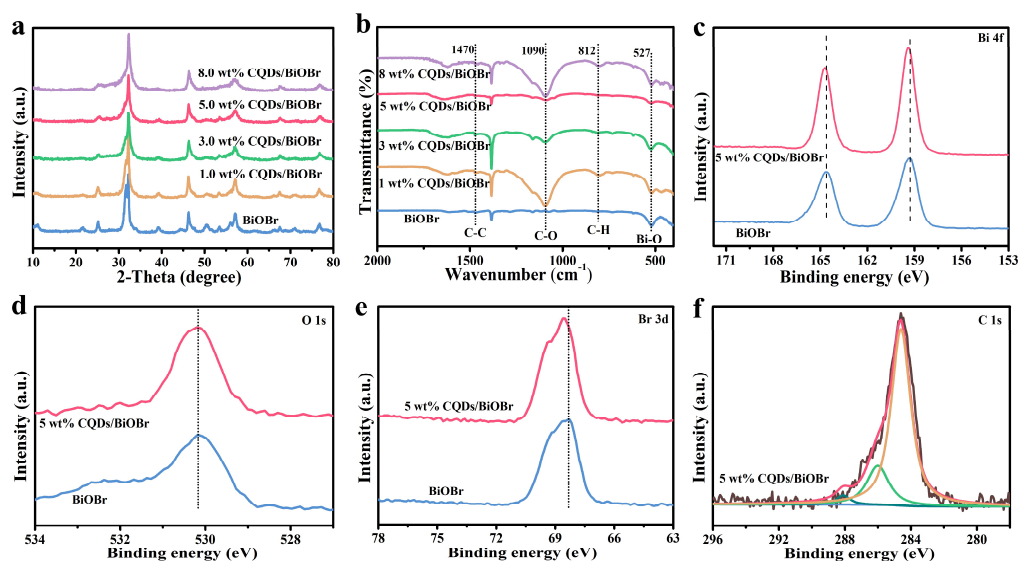


Figure 1. (a) XRD patterns, (b) FT-IR spectra of as-prepared samples, XPS spectra of (c) Bi $4f$, (d) O $1s$, (e) Br $3d$ and (f) C $1s$.

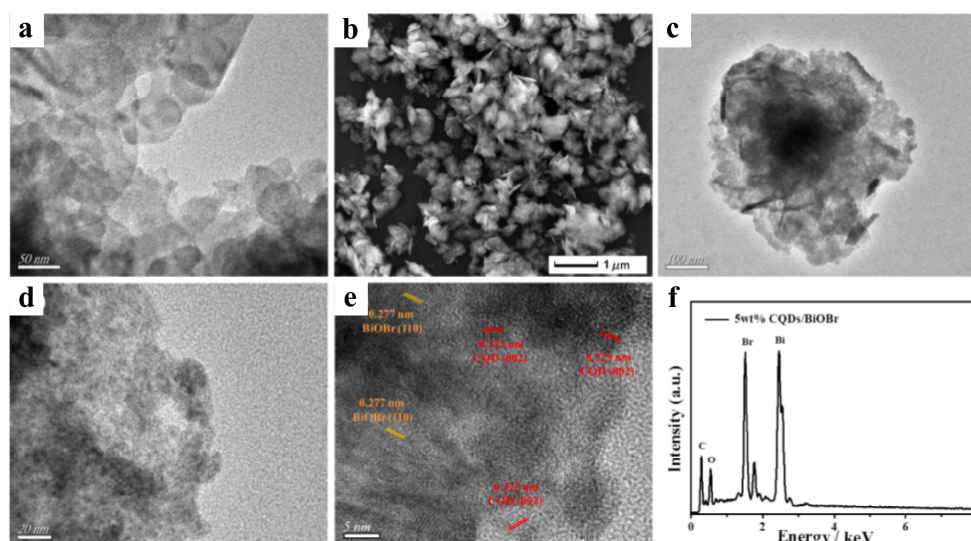


Figure 2. (a) TEM image of BiOBr, (b) SEM image, (c, d) TEM image and (e) HRTEM image of 5.0 wt% CQDs/BiOBr material, (f) EDS of the 5.0 wt% CQDs/BiOBr composite.

served in Figure 2d. The CQDs were evenly distributed in BiOBr. Figure 2e is the HRTEM diagram of the composites. The lattice fringe spacing of BiOBr and CQDs could be observed. The lattice spacing of 0.277 and 0.323 nm corresponded to the (110) plane of BiOBr and the (002) plane of CQDs, respectively. This result showed that CQDs/BiOBr composite photocatalytic materials were successfully synthesized in situ by mechanical ball milling. Furthermore, the EDS of 5.0 wt% CQDs/BiOBr composite was performed to study the elemental composition and distribution. Figure 2f indicates that the prepared sample was composed of Bi, O, Br and C. Figure S2 is the element mapping images of the 5.0 wt% CQDs/BiOBr composite. It is confirmed that the sample was the presence of four elements: Bi, O, Br and C evenly scattered in the CQDs/BiOBr composites. These results of XRD, FT-IR, XPS, SEM and TEM all confirmed the successful preparation of CQDs/BiOBr complexes.

The specific surface areas of as-prepared photocatalysts were measured by the nitrogen adsorption-desorption isotherm. The specific surface area of the BiOBr monomer was $4.64 \text{ m}^2\text{g}^{-1}$ from Figure 3a. When CQDs were introduced to composites, the specific surface area of 5.0 wt% CQDs/BiOBr being $37.93 \text{ m}^2\text{g}^{-1}$ increased substantially (Figure 3b). This ultra-thin nanosheet exposed a larger surface area and improved material utilization compared to other bulk materials. In addition, a larger specific surface areas could not only help to capture sunlight, but also provide more active sites to adsorb more organic pollutants to participate in the photocatalytic process. Photocatalytic properties could be greatly improved because of these physical characteristics.^[41] In this work, the specific surface area of the photocatalysts was an important factor impacting the photocatalytic properties.

In the whole process of degradation reaction for pollutants, the more visible light was absorbed by the materials, the more solar energy could be converted into chemical energy, which could promote the degradation of organic pollutants. For the sake of studying the optical properties of composites, the prepared materials

were checked based on UV-vis DRS, with the result exhibited in Figure 3c. The maximum absorption edge of BiOBr was about 430 nm. After introducing CQDs, the absorption edge exhibited red shift in all composite materials, and the light absorption capacity of the composites was significantly enhanced in the range of visible light. This result demonstrated that coupling CQDs with BiOBr could improve the visible light utilization. As seen from Figure 3d, the band gap (E_g) of BiOBr monomer was computed by $h\nu = A(h\nu - E_g)^{1/2}$. The $(\alpha E_{\text{photon}})^{1/2}$ vs. E_{photon} curve of BiOBr monomer was computed by the classic Tauc approach. The E_g of BiOBr monomer was nearly 2.22 eV.

Nowadays, TC antibiotics are widely used in the treatment of human diseases due to their low price and strong inhibitory effects on pathogenic bacteria. However, the abuse of TC causes serious environmental pollution problems. It is difficult to eliminate TC in nature due to its stable structure. The residual TC in water is

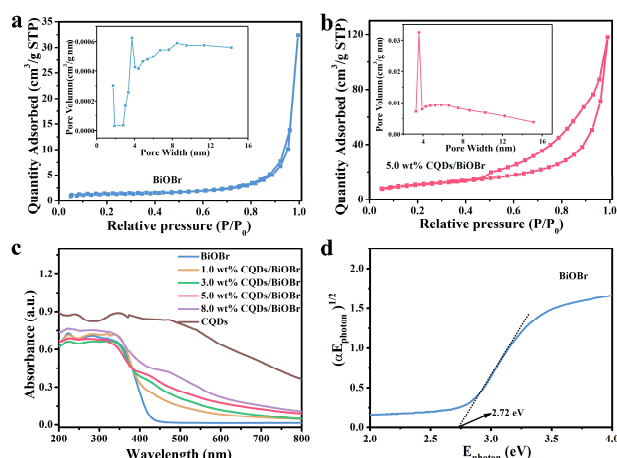


Figure 3. Nitrogen adsorption-desorption isotherms of (a) pure BiOBr, (b) 1.0 wt% CQDs/BiOBr materials, (c) UV-vis DRS of the as-prepared materials, (d) $(\alpha E_{\text{photon}})^{1/2}$ vs. E_{photon} curve of the as-prepared BiOBr samples.

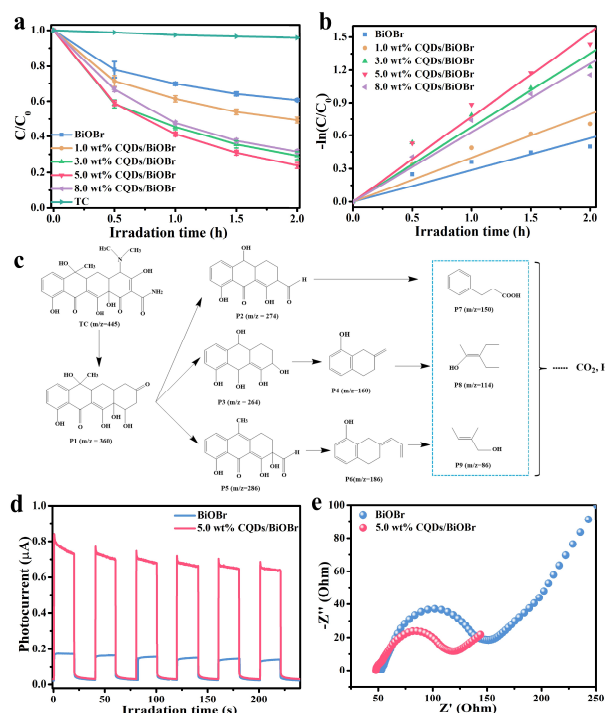


Figure 4. (a) Photocatalytic performance of as-prepared samples for the degradation of TC under visible light irradiation, (b) Reaction kinetics for the degradation of TC, (c) Possible degradation pathways of TC. (d) Transient photocurrent, (e) EIS of pure BiOBr and 5.0 wt% CQDs/BiOBr material.

transmitted to the human body through different paths, which causes a serious threat to human health. It is very necessary to degrade the residual TC in the environment. Therefore, TC was chosen to do photocatalytic degradation experiments to assess the performance of prepared photocatalysts. As obviously shown in Figure 4a, TC was hardly degraded without the presence of photocatalyst, which indicated the self-degradation of TC could be insignificant. From the degradation curves, all the CQDs/BiOBr composites showed significant better performance of degradation than BiOBr monomer, which indicated introducing CQDs could effectively improve the photocatalytic performance of BiOBr. Notably, with the increase of CQDs, the degradation efficiency showed a trend of first increase and then decrease because excessive CQDs might cover the active sites of BiOBr. About 40% of TC solution was degraded by BiOBr after 120 min, while the 5.0 wt% CQDs/BiOBr performing the highest performance in the composites could degrade 76% of TC. Meanwhile, the kinetics of photocatalytic degradation of TC by prepared samples was researched. As seen from the first order kinetic curves (Figure 4b), the degradation rate of composites was significantly improved after introducing CQDs. The degradation rate of 5.0 wt% CQDs/BiOBr performing the best activity was 0.7707 h^{-1} , which was three times higher than that of BiOBr monomer. In addition, the BiOBr and 5 wt% CQDs/BiOBr composites were synthesized by different methods (hydrothermal and physical mixing methods) and by different Br sources (KBr) and then performed the photocatalytic

performance tests. As shown in Figure S3 and S4, after 120 min of irradiation, 5%, 13%, 27% and 58% of TC were photodegraded by BiOBr-K, 5 wt% CQDs/BiOBr-PM, BiOBr-H and 5 wt% CQDs/BiOBr-H. Meanwhile, the commercial Bi_2O_3 only degraded 9% of TC after 120 min of irradiation. The photocatalytic degradation properties of BiOBr and 5 wt% CQDs/BiOBr materials synthesized by the ionic liquid assisted mechanical ball milling were much higher than that of these photocatalysts (Bi_2O_3 , BiOBr-K, BiOBr-H, 5 wt% CQDs/BiOBr-PM and 5 wt% CQDs/BiOBr-H).

To further investigate the TC degradation process, the intermediates were detected by LC-MS. Figure S5 is the mass spectra of TC solution, which suggests that many intermediates are produced during the degradation process. The possible degradation pathways are proposed based on these intermediates. As shown in Figure 4c, TC ($m/z = 445$) with electron-rich functional groups is firstly attacked by the reactive species to form intermediate P1 ($m/z = 360$) by the elimination of amide group and demethylation. P1 is further transformed into P2 ($m/z = 274$), P3 ($m/z = 264$), and P5 ($m/z = 286$) by ring opening reaction, demethylation, and dehydroxylation. P3 is further converted into P4 ($m/z = 160$) by ring opening reaction and dehydroxylation. P5 is further converted into P6 ($m/z = 186$) by demethylation, ring opening reaction and dehydroxylation. After further suffering from the attacking of $\text{O}_2^{\cdot-}$, $\cdot\text{OH}$ and h^+ , P2, P4, and P6 are decomposed into smaller molecules P7 ($m/z = 150$), P8 ($m/z = 114$), and P9 ($m/z = 86$) which finally are gradually mineralized into CO_2 and H_2O .

The transient photocurrents and EIS were measured to explore the separation and transmission efficiency of photo-induced charges of BiOBr and the CQDs/BiOBr composites.^[42,43] Figure 4d shows the photocurrent responses of BiOBr and 5.0 wt% CQDs/BiOBr composite. The photocurrent response of 5.0 wt% CQDs/BiOBr composite is higher than that of BiOBr. The greater the photocurrent intensity is, the higher the photogenerated carrier separation efficiency of the material will be. It suggests that the 5.0 wt% CQDs/BiOBr composites exhibited a higher separation efficiency of photogenerated charges. We speculate that the electrons excited by the light were rapidly transferred to the surface of CQDs, which prevented the recombination of electron-hole pairs. At the same time, EIS was used to study the charge-transport capability of the materials. The diameter of Nyquist semi-circle arc of 5.0 wt% CQDs/BiOBr is smaller than that of BiOBr in Figure 4e. This indicated that the resistance of the composite material after the introduction of CQDs decreased and the efficiency of charge transmission accelerated. The above results showed that introducing CQDs to the BiOBr could effectively promote the photo-induced charge separation and transfer.

The stability of catalysts is a vital indicator to evaluate the potential industrial application prospects of materials. The stability of CQDs/BiOBr composites was evaluated through cycling experiment under visible light. As could be seen from Figure S6a, the performance of 5.0 wt% CQDs/BiOBr was slightly down after five cycling photocatalytic experiment, which indicated the composite has good stability. Furthermore, Figure S6b shows the XRD patterns of 5.0 wt% CQDs/BiOBr composite before and after five cycling experiments. Though the intensity of characteristic peaks became weak, there are no new peaks appearing and peak shift,

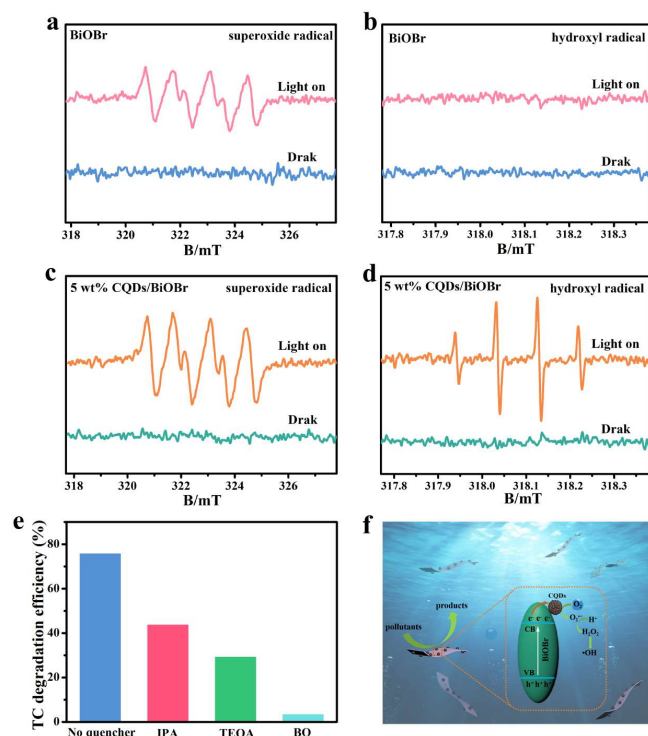


Figure 5. ESR spectra of DMPO- $\text{O}_2^{\cdot-}$ and DMPO- $\cdot\text{OH}$ of (a, b) BiOBr and (c, d) 5.0 wt% CQDs/BiOBr, (e) Photocatalytic degradation performances of TC in the presence of different radical scavengers, (f) Possible mechanism of 5.0 wt% CQDs/BiOBr composite for photocatalytic degradation.

illustrating that the crystal structure of the samples is stable. Above results all confirmed the photocatalytic performance and crystal structures of CQDs/BiOBr materials are stable.

The ESR characterization was used to prove the presence of DMPO- $\text{O}_2^{\cdot-}$ and DMPO- $\cdot\text{OH}$ produced by prepared materials during the degradation process.^[44] As shown in Figure 5a-d, no characteristic peaks were observed in the ESR profiles of the monomer and the composite under dark reaction conditions, so the system cannot produce active species in the dark. Under the existence of light, the four strong representative peaks of DMPO- $\text{O}_2^{\cdot-}$ were present in both BiOBr monomer and 5.0 wt% CQDs/BiOBr composite, and the signal peak intensity of 5.0 wt% CQDs/BiOBr composite was significantly higher than that of BiOBr monomer. This suggested that the 5.0 wt% CQDs/BiOBr could produce more $\text{O}_2^{\cdot-}$ under light radiation. The possible reason was that transferring electrons excited to CQDs avoided the combination of photogenerated electrons and holes on the surface of BiOBr, thus improving the utilization of photo-induced charges. More electrons reduced O_2 to $\text{O}_2^{\cdot-}$. No signal peaks of DMPO- $\cdot\text{OH}$ were found for BiOBr monomer under light irradiation because the valence band (VB) position of BiOBr is more negative than that of $\text{E}^0(\cdot\text{OH}/\text{OH}^{\cdot})$ (2.38 eV vs. NHE). While 5.0 wt% CQDs/BiOBr exhibited four obvious characteristic peaks of DMPO- $\cdot\text{OH}$, which indicated the 5.0 wt% CQDs/BiOBr could produce $\cdot\text{OH}$ under visible light. The ESR results illustrated $\text{O}_2^{\cdot-}$ and $\cdot\text{OH}$ were produced, which played a significant role in the photocatalytic reaction.

For ulteriorly confirming the active species during photocatalytic reaction, the free radical capture experiment was carried out on 5.0 wt% CQDs/BiOBr. BQ, IPA and TEOA were added to TC solution as $\text{O}_2^{\cdot-}$, $\cdot\text{OH}$ and h^+ capture agents, respectively. The photocatalytic degradation experiments in the presence of different quenchers are shown in Figure 5e. TC was hardly degraded after adding BQ to the reaction, which indicated that $\text{O}_2^{\cdot-}$ played a major role in the degradation process. When IPA and TEOA were added to the reaction, the degradation efficiency of TC was significantly reduced, indicating that OH and h^+ were also produced during the degradation process. The results of radical capture experiments confirmed that the free radicals produced by CQDs/BiOBr during photocatalysis were $\text{O}_2^{\cdot-}$, $\cdot\text{OH}$ and h^+ with their contribution ability as follows: $\text{O}_2^{\cdot-} > \text{h}^+ > \cdot\text{OH}$.

To explore the separation and transfer process of photogenerated carriers in this system, XPS valence band spectrum and UV-vis DRS analysis aimed to compute the positions of energy band for BiOBr. In Figure S7, the VB position of BiOBr monomer by measuring was 2.06 eV. The E_g of the BiOBr monomer was known to be 2.72 eV. The conduction band (CB) of BiOBr was about -0.66 eV by calculation based on $E_{\text{CB}} = E_{\text{VB}} - E_g$. Therefore, the E_{CB} position of BiOBr was more negative than that of $\text{E}^0(\text{O}_2/\text{O}_2^{\cdot-})$ (-0.046 eV vs. NHE), and the electrons on its CB were able to reduce O_2 to generate $\text{O}_2^{\cdot-}$. While the position of $\text{E}^0(\cdot\text{OH}/\text{OH}^{\cdot})$ is 2.38 eV, the higher VB position of BiOBr prevented the hole from oxidizing OH^- to $\cdot\text{OH}$. The obtained conclusions differed from the above result of ESR analysis and free radical capture experiments. The possible reason for this result was that H_2O_2 was generated in the solution and then produced the $\cdot\text{OH}$. CQDs possessed excellent interface electron transfer capability, which enabled electrons on the BiOBr CB to transfer to CQDs rapidly and effectively inhibited the combination of photogenerated electron-hole pairs. Thereby, more electrons were involved in the reduction reaction, and oxygen was reduced to produce $\text{O}_2^{\cdot-}$. The part of $\text{O}_2^{\cdot-}$ would further react with the hydrogen ions to generate H_2O_2 which decomposed into $\cdot\text{OH}$ gradually.

According to characterization analysis and experimental results, the degradation mechanism of CQDs/BiOBr photocatalytic materials was proposed during the process of photocatalytic degradation. As shown in Figure 5f, electrons were excited by visible light to migrate from VB to the CB of BiOBr and generate holes in the VB of BiOBr. Photogenerated holes could directly degrade pollutants. Photogenerated electrons were rapidly transferred to CQDs because CQDs possessed excellent transfer ability of interfacial charge. The introducing of CQDs realized the speedy separation of photo-induced charges and effectively prevent their combinations. The collective electrons on CQDs could reduce O_2 to $\text{O}_2^{\cdot-}$ which possessed a strong oxidation capacity. The part of $\text{O}_2^{\cdot-}$ would further react with the hydrogen ions in the solution and generate H_2O_2 . H_2O_2 slowly decomposed into $\cdot\text{OH}$ because H_2O_2 was less stable. The organic pollutants adsorbed on the surface of photocatalysts were oxidized directly by the formed active species including $\text{O}_2^{\cdot-}$, $\cdot\text{OH}$ and h^+ . Pollutants underwent a series of complex oxidation processes, and were eventually decomposed into H_2O and CO_2 .

CONCLUSION

In summary, CQDs/BiOBr photocatalysts were synthesized in situ by ionic liquid assisted mechanical ball milling method. Compared with other synthetic methods, both BiOBr and CQDs/BiOBr composites prepared via ionic liquid assisted mechanical ball milling method exhibit higher photocatalytic degradation properties. Furthermore, the introduction of CQDs significantly enhanced the photocatalytic degradation performance of BiOBr. The degradation rate of TC in the optimized CQDs/BiOBr material is three times higher than that of pure BiOBr because CQDs could rapidly transfer photo-induced electrons and avoid the combination of photogenerated electrons and holes. The photocatalytic mechanism was proposed and discussed in detail based on the energy band position and active species. This work provides a reference scheme for enhancing the performance of photocatalyst to handle environmental pollution problems.

■ EXPERIMENTAL

Materials and Synthesis. In this work, all reagents were analytical pure reagents and used directly without further purification. In the whole experimental process, distilled water was used to configure the solution. $\text{Bi}(\text{NO}_3)_3 \cdot 5\text{H}_2\text{O}$, citric acid and ethanediamine were purchased from Sinopharm Chemical Reagent Co., Ltd. 1-Hexadecyl-3-methylimidazolium bromine ($[\text{C}_{16}\text{mim}]\text{Br}$) was commercially available from Shanghai Chengjie Chemical Co. Ltd.

The synthetic method of CQDs referred to the literature,^[45] and the specific steps were as follows: firstly, 5 mmol citric acid was mixed into 10 mL distilled water, followed by adding 335 μL ethylenediamine. The solution was stirred at a uniform speed for half an hour. Then, the stirred solution was poured into a 25 mL Teflon-lined autoclave and heated in a 200 °C oven for 5 h. After that, the dark brown solution obtained after natural cooling was poured into the dialysis bag followed by dialysis in distilled water for 24 h to remove the existing macromolecular impurities. Finally, the material was freeze-dried in the freeze drier, obtaining CQDs.

The synthesis of BiOBr: 1 mmol $\text{Bi}(\text{NO}_3)_3 \cdot 5\text{H}_2\text{O}$ and 1 mmol $[\text{C}_{16}\text{mim}]\text{Br}$ were mixed into an agate ball milling tank with a volume of 50 mL. The ball mill ran at 1200 rpm for 60 min under normal temperature and pressure. The samples thus obtained were directly washed with distilled water and ethanol for three times and dried at 60 °C for 10 h. The final sample was BiOBr.

The synthesis of CQDs/BiOBr composites: 1 mmol $\text{Bi}(\text{NO}_3)_3 \cdot 5\text{H}_2\text{O}$, 1 mmol $[\text{C}_{16}\text{mim}]\text{Br}$ and a certain amount of CQDs were mixed into an agate ball milling tank with a volume of 50 mL. The ball mill ran at 1200 rpm for 60 min under normal temperature and pressure. The samples obtained by ball milling was directly washed with distilled water and ethanol for three times and dried at 60 °C for 10 h. The final orange samples were CQDs/BiOBr composites. In the process of material synthesis, 1.0, 3.0, 5.0 and 8.0 wt% CQDs/BiOBr composites were obtained by controlling the amount of CQDs, respectively.

Characterization of Photocatalysts. X-ray diffraction (XRD) was carried out on a Shimadzu XRD-6000 X-ray diffractometer with Cu-K α irradiation from 10° to 80°. The element composition and surface chemical states of the prepared material were investigated using X-ray photoelectron spectroscopy (XPS), which

were measured on a VG MultiLab 2000 system. Scanning electron microscopy (SEM, JOEL JSM-7001) and transmission electron microscopy (TEM, JEOL JSM-2100) were used to study the outer morphologies and microstructures of the catalysts. UV-vis diffuse reflectance spectra (UV-vis DRS) of the prepared samples were obtained by using a UV-2450 spectrophotometer (Shimadzu Corporation, Japan). A Tristar II 3020 surface area and porosity analyzer were used to investigate the specific surface area of the samples. The intermediates were analyzed by LC-MS (Thermo, *thermo LXQ LC/MS). Electrochemical impedance spectroscopy (EIS) and photocurrent were measured on electrochemical workstation (CHI760B, Chenhua Instrument Company, Shanghai, China).

Photocatalytic Experiments. The specific experimental operation steps were as follows: 50 mg of photocatalyst was weighed in Pyrex glass reaction bottle and scattered into the solution of TC (100 mL, 20 mgL^{-1}). At the same time, the air pump was used to provide ample oxygen for the reaction. The system of cyclic water was running to ensure that the reaction temperature is constant at 30 °C. The photocatalytic reaction was performed in a photo-reactor with the xenon lamp. Prior to light irradiation, the miscible liquid was stirred in the absence of visible light for half an hour to achieve an adsorption-desorption equilibrium. Then the xenon lamp was turned on for the light reaction. About 5 mL of solution was extracted every 0.5 h during the catalytic reaction. The particles of samples in the suspension were removed by centrifugation. The filtered solution was used for further test and analysis. The photocatalytic degradation efficiency was determined by the concentration of TC measured at 356 nm using UV-visible spectrophotometer.

Photoelectrochemical Measurement. To study the photoelectrochemical properties of photocatalytic materials, an electrochemical analyzer equipped with a standard three-electrode system needed to be used. 4 mg photocatalyst was smeared to ITO sheets (the area was 0.5 cm^2) as the working electrode. Counter electrode was prepared from the platinum sheet. Ag/AgCl electrode was used as reference electrode. The photocurrent measurements were performed in the solution of phosphate buffered saline (0.1 M, pH = 7.0) using 500 W Xenon lamp. EIS were performed in the solution of 0.1 M KCl and 5 mM $\text{Fe}(\text{CN})_6^{3-}/\text{Fe}(\text{CN})_6^{4-}$.

■ ACKNOWLEDGEMENTS

This work was financially supported by the National Natural Science Foundation of China (Nos. 22108106, 22108108, 22109055, 21878134), Natural Science Foundation of Jiangsu Province (BK20210742), China Postdoctoral Science Foundation (No. 2020M680065), Hong Kong Scholar Program (No. XJ2021021) and Key Laboratory of Electrochemical Energy Storage and Energy Conversion of Hainan Province (No. KFKT2021005).

■ AUTHOR INFORMATION

Corresponding authors. Emails: Liupj12@126.com and xjx@ujs.edu.cn

■ COMPETING INTERESTS

The authors declare no competing interests.

■ ADDITIONAL INFORMATION

Supplementary information is available for this paper at
<http://manu30.magtech.com.cn/jghx/EN/10.14102/j.cnki.0254-5861.2022-0141>

For submission: <https://mc03.manuscriptcentral.com/cjsc>

■ REFERENCES

- (1) Wang, Z.; Chen, M.; Huang, D.; Zeng, G.; Xu, P.; Zhou, C.; Lai, C.; Wang, H.; Cheng, M.; Wang, W. Multiply structural optimized strategies for bismuth oxyhalide photocatalysis and their environmental application. *Chem. Eng. J.* **2019**, 374, 1025-1045.
- (2) Jin, X.; Ye, L.; Xie, H.; Chen, G. Bismuth-rich bismuth oxyhalides for environmental and energy photocatalysis. *Coord. Chem. Rev.* **2017**, 349, 84-101.
- (3) Yang, Y.; Zhang, C.; Lai, C.; Zeng, G.; Huang, D.; Cheng, M.; Wang, J.; Chen, F.; Zhou, C.; Xiong, W. BiOX (X = Cl, Br, I) photocatalytic nano-materials: applications for fuels and environmental management. *Adv. Colloid Interface Sci.* **2018**, 254, 76-93.
- (4) Meng, L.; Qu, Y.; Jing, L. Recent advances in BiOBr-based photocatalysts for environmental remediation. *Chin. Chem. Lett.* **2021**, 32, 3265-3276.
- (5) Cheng, H.; Huang, B.; Dai, Y. Engineering BiOX (X = Cl, Br, I) nanostructures for highly efficient photocatalytic applications. *Nanoscale* **2014**, 6, 2009-2026.
- (6) Anwer, H.; Mahmood, A.; Lee, J.; Kim, K. H.; Park, J. W.; Yip, A. C. K. Photocatalysts for degradation of dyes in industrial effluents: opportunities and challenges. *Nano Res.* **2019**, 12, 955-972.
- (7) Yao, L.; Yang, H.; Chen, Z.; Qiu, M.; Hu, B.; Wang, X. Bismuth oxychloride-based materials for the removal of organic pollutants in wastewater. *Chemosphere* **2021**, 273, 128576.
- (8) Su, X.; Fan, D.; Sun, H.; Yang, J.; Yu, Z.; Zhang, D.; Pu, X.; Li, H.; Cai, P. One-dimensional rod-shaped Ag₂Mo₂O₇/BiOI n-n junctions for efficient photodegradation of tetracycline and rhodamine B under visible light. *J. Alloys Compd.* **2022**, 912, 165184.
- (9) Jiang, X.; Kong, D.; Luo, B.; Wang, M.; Zhang, D.; Pu, X. Preparation of magnetically retrievable flower-like AgBr/BiOBr/NiFe₂O₄ direct Z-scheme heterojunction photocatalyst with enhanced visible-light photoactivity. *Colloids Surf., A* **2022**, 633, 127880.
- (10) Sharma, K.; Dutta, V.; Sharma, S.; Raizada, P.; Hosseini-Bandegharai, A.; Thakur, P.; Singh, P. Recent advances in enhanced photocatalytic activity of bismuth oxyhalides for efficient photocatalysis of organic pollutants in water: a review. *J. Ind. Eng. Chem.* **2019**, 78, 1-20.
- (11) Wang, C.; Du, P.; Duan, X.; Luo, L.; Li, W. Tailoring of visible light driven photocatalytic activities of flower-like BiOBr microparticles towards wastewater purification application. *Adv. Mater. Interfaces* **2022**, 9, 2101671.
- (12) Ji, M.; Zhang, Z.; Xia, J.; Di, J.; Liu, Y.; Chen, R.; Yin, S.; Zhang, S.; Li, H. Enhanced photocatalytic performance of carbon quantum dots/BiOBr composite and mechanism investigation. *Chin. Chem. Lett.* **2018**, 29, 805-810.
- (13) Meng, J.; Duan, Y.; Jing, S.; Ma, J.; Wang, K.; Zhou, K.; Ban, C.; Wang, Y.; Hu, B.; Yu, D.; Gan, L. Facet junction of BiOBr nanosheets boosting spatial charge separation for CO₂ photoreduction. *Nano Energy* **2022**, 92, 106671.
- (14) Shi, M.; Li, G.; Li, J.; Jin, X.; Tao, X.; Zeng, B.; Pidko, E. A.; Li, R.; Li, C. Intrinsic facet-dependent reactivity of well-defined BiOBr nanosheets on photocatalytic water splitting. *Angew. Chem., Int. Ed.* **2020**, 59, 6590-6595.
- (15) Wu, J.; Li, X.; Shi, W.; Ling, P.; Sun, Y.; Jiao, X.; Gao, S.; Liang, L.; Xu, J.; Yan, W.; Wang, C.; Xie, Y. Efficient visible-light-driven CO₂ reduction realized by defect-mediated BiOBr atomic layers. *Angew. Chem., Int. Ed.* **2018**, 57, 8719-8723.
- (16) Zhang, H.; Zhao, L.; Wang, L.; Hao, J.; Meng, X. Fabrication of oxygen-vacancy-rich black-BiOBr/BiOBr heterojunction with enhanced photocatalytic activity. *J. Mater. Sci.* **2020**, 55, 10785-10795.
- (17) Wang, B.; Yang, S.; Chen, H.; Gao, Q.; Weng, Y.; Zhu, W.; Liu, G.; Zhang, Y.; Ye, Y.; Zhu, H.; Li, H.; Xia, J. Revealing the role of oxygen vacancies in bimetallic PbBiO₂Br atomic layers for boosting photocatalytic CO₂ conversion. *Appl. Catal. B* **2020**, 277, 119170.
- (18) Zhang, W.; Peng, Y.; Yang, Y.; Zhang, L.; Bian, Z.; Wang, H. Bismuth-rich strategy intensifies the molecular oxygen activation and internal electrical field for the photocatalytic degradation of tetracycline hydrochloride. *Chem. Eng. J.* **2022**, 430, 132963.
- (19) Jin, X.; Lv, C.; Zhou, X.; Xie, H.; Sun, S.; Liu, Y.; Meng, Q.; Chen, G. A bismuth rich hollow Bi₄O₅Br₂ photocatalyst enables dramatic CO₂ reduction activity. *Nano Energy* **2019**, 64, 103955.
- (20) Wilczewska, P.; Bielicka-Gieldorń, A.; Szczodrowski, K.; Malankowska, A.; Ryl, J.; Tabaka, K.; Siedlecka, E. M. Morphology regulation mechanism and enhancement of photocatalytic performance of BiOX (X = Cl, Br, I) via mannitol-assisted synthesis. *Catalysts* **2021**, 11, 312.
- (21) Shi, M.; Li, G.; Li, J.; Jin, X.; Tao, X.; Zeng, B.; Pidko, E. A.; Li, R.; Li, C. Intrinsic facet-dependent reactivity of well-defined BiOBr nanosheets on photocatalytic water splitting. *Angew. Chem., Int. Ed.* **2020**, 59, 6590-6595.
- (22) Zhao, Y.; Li, Z.; Wei, J.; Li, X.; Shi, H.; Cao, B.; Fan, J. Efficient photodegradation of cefixime catalyzed by a direct Z-scheme CQDs-BiOBr/CN composite: performance, toxicity evaluation and photocatalytic mechanism. *Chemosphere* **2022**, 292, 133430.
- (23) Wang, B.; Zhang, W.; Liu, G.; Chen, H.; Weng, Y.; Li, H.; Chu, P.; Xia, J. Excited electron-rich Bi^{(3-x)+} sites: a quantum well-like structure for highly-promoted selective photocatalytic CO₂ reduction performance. *Adv. Funct. Mater.* **2022**, 202202885.
- (24) Lv, X.; Yan, D. Y. S.; Lam, F. L. Y.; Ng, Y. H.; Yin, S.; An, A. K. Solvothermal synthesis of copper-doped BiOBr microflowers with enhanced adsorption and visible-light driven photocatalytic degradation of norfloxacin. *Chem. Eng. J.* **2020**, 401, 126012.
- (25) Ren, X.; Gao, M.; Zhang, Y.; Zhang, Z.; Cao, X.; Wang, B.; Wang, X. Photocatalytic reduction of CO₂ on BiOX: effect of halogen element type and surface oxygen vacancy mediated mechanism. *Appl. Catal. B* **2020**, 274, 119063.
- (26) Chen, X.; Zhang, X.; Li, Y.; Qi, M.; Li, J.; Tang, Z.; Zhou, Z.; Xu, Y. Transition metal doping BiOBr nanosheets with oxygen vacancy and exposed {102} facets for visible light nitrogen fixation. *Appl. Catal. B* **2021**, 281, 119516.
- (27) Mao, S.; Zou, Y.; Sun, G.; Zeng, L.; Wang, Z.; Ma, D.; Guo, Y.; Cheng, Y.; Wang, C.; Shi, J. Thio linkage between CdS quantum dots and UiO-66-type MOFs as an effective transfer bridge of charge carriers boosting visible-light-driven photocatalytic hydrogen production. *J. Colloid Interface Sci.* **2021**, 581, 1-10.
- (28) Shi, J.; Sun, D.; Zou, Y.; Ma, D.; He, C.; Jia, X.; Niu, C. Trap-level-tunable Se doped CdS quantum dots with excellent hydrogen evolution performance without co-catalyst. *Chem. Eng. J.* **2019**, 364, 11-19.
- (29) Kou, J.; Lu, C.; Wang, J.; Chen, Y.; Xu, Z.; Varma, R. S. Selectivity

enhancement in heterogeneous photocatalytic transformations. *Chem. Rev.* **2017**, 117, 1445-1514.

(30) Syed, N.; Huang, J.; Feng, Y. CQDs as emerging trends for future prospect in enhancement of photocatalytic activity. *Carbon Lett* **2022**, 32, 81-97.

(31) Zhang, Y.; Zhao, Y.; Xu, Z.; Su, H.; Bian, X.; Zhang, S.; Dong, X.; Zeng, L.; Zeng, T.; Feng, M.; Li, L.; Sharma, V. K. Carbon quantum dots implanted CdS nanosheets: efficient visible-light driven photocatalytic reduction of Cr(VI) under saline conditions. *Appl. Catal. B* **2020**, 262, 118306.

(32) Preeyanghaa, M.; Vinesh, V.; Sabarikirishwaran, P.; Rajkamal, A.; Ashokkumar, M.; Neppolian, B. Investigating the role of ultrasound in improving the photocatalytic ability of CQD decorated boron-doped g-C₃N₄ for tetracycline degradation and first-principles study of nitrogen-vacancy formation. *Carbon* **2022**, 192, 405-417.

(33) Lin, Y.; Peng, C.; Lim, S.; Chen, C.; Nguyễn, T.; Wang, T.; Lin, M.; Hsu, Y.; Chen, S.; Lin, Y. Tailoring the surface oxygen engineering of a carbon-quantum-dot-sensitized ZnO@H-ZnO_{1-x} multijunction toward efficient charge dynamics and photoactivity enhancement. *Appl. Catal. B* **2021**, 285, 119846.

(34) Zhou, Q.; Huang, W.; Xu, C.; Liu, X.; Yang, K.; Li, D.; Hou, Y.; Dionysiou, D. D. Novel hierarchical carbon quantum dots-decorated BiOCl nanosheet/carbonized eggshell membrane composites for improved removal of organic contaminants from water via synergistic adsorption and photocatalysis. *Chem. Eng. J.* **2021**, 420, 129582.

(35) Zhao, C.; Liang, Y.; Li, W.; Tian, Y.; Chen, X.; Yin, D.; Zhang, Q. BiOBr/BiOCl/carbon quantum dot microspheres with superior visible light-driven photocatalysis. *RSC Adv.* **2017**, 7, 52614-52620.

(36) Sun, J.; Li, X.; Zhao, Q.; Liu, B. Ultrathin nanoflake-assembled hierarchical BiOBr microflower with highly exposed {001} facets for efficient photocatalytic degradation of gaseous ortho-dichlorobenzene. *Appl. Catal. B* **2021**, 281, 119478.

(37) Kahoush, M.; Behary, N.; Cayla, A.; Mutel, B.; Guan, J.; Nierstrasz, V. Surface modification of carbon felt by cold remote plasma for glucose oxidase enzyme immobilization. *Appl. Surf. Sci.* **2019**, 476, 1016-1024.

(38) Wang, B.; Di, J.; Lu, L.; Yan, S.; Liu, G.; Ye, Y.; Li, H.; Zhu, W.; Li, H.; Xia, J. Sacrificing ionic liquid-assisted anchoring of carbonized polymer

dots on perovskite-like PbBiO₂Br for robust CO₂ photoreduction. *Appl. Catal. B* **2019**, 254, 551-559.

(39) Tang, L.; Lv, Z.; Xue, Y.; Xu, L.; Qiu, W.; Zheng, C.; Chen, W.; Wu, M. MIL-53 (Fe) incorporated in the lamellar BiOBr: promoting the visible-light catalytic capability on the degradation of rhodamine B and carbamazepine. *Chem. Eng. J.* **2019**, 374, 975-982.

(40) Jiao, W.; Xie, Y.; He, F.; Wang, K.; Ling, Y.; Hu, Y.; Wang, J.; Ye, H.; Wu, J.; Hou, Y. A visible light-response flower-like La-doped BiOBr nanosheets with enhanced performance for photoreducing CO₂ to CH₃OH. *Chem. Eng. J.* **2021**, 418, 129286.

(41) Wang, B.; Zhao, J.; Chen, H.; Weng, Y.; Tang, H.; Chen, Z.; Zhu, W.; She, Y.; Xia, J.; Li, H. Unique Z-scheme carbonized polymer dots/Bi₄O₅Br₂ hybrids for efficiently boosting photocatalytic CO₂ reduction. *Appl. Catal. B* **2021**, 293, 120182.

(42) Dong, J.; Chen, F.; Xu, L.; Yan, P.; Qian, J.; Chen, Y.; Yang, M.; Li, H. Fabrication of sensitive photoelectrochemical aptasensor using Ag nanoparticles sensitized bismuth oxyiodide for determination of chloramphenicol. *Microchem. J.* **2022**, 178, 107317.

(43) Fu, X.; Wang, J.; Hu, X.; He, K.; Tu, Q.; Yue, Q.; Kang, Y. Scalable chemical interface confinement reduction BiOBr to bismuth porous nanosheets for electroreduction of carbon dioxide to liquid fuel. *Adv. Funct. Mater.* **2022**, 32, 2107182.

(44) Zhang, Z.; Li, L.; Jiang, Y.; Xu, J. Step-scheme photocatalyst of CsPbBr₃ quantum Dots/BiOBr nanosheets for efficient CO₂ photoreduction. *Inorg. Chem.* **2022**, 61, 3351-3360.

(45) Zhu, S.; Meng, Q.; Wang, L.; Zhang, J.; Song, Y.; Jin, H.; Zhang, K.; Sun, H.; Wang, H.; Yang, B. Highly photoluminescent carbon dots for multicolor patterning, sensors, and bioimaging. *Angew. Chem., Int. Ed.* **2013**, 52, 3953-3957.

Received: May 27, 2022

Accepted: July 1, 2022

Published online: July 14, 2022

Published: July 25, 2022